

Highlights

An Information-Theoretic Framework for Optimal Experimental Design in Magnetic Nanoparticle Hyperthermia

Mahesh Nandyala, Andrew Lanham, Prashant K. Jha, Chengyue Wu, John D. Hazle, Thomas E. Yankeelov, R Jason Stafford, Ahmed A. El-Gendy, David Fuentes

- Information-theoretic framework optimizes magnetic nanoparticle hyperthermia planning
- Optimization maximizes mutual information to reduce parameter uncertainty
- Framework handles one or multiple uncertain parameters with stable convergence

An Information-Theoretic Framework for Optimal Experimental Design in Magnetic Nanoparticle Hyperthermia

Mahesh Nandyala^{a,b,*}, Andrew Lanham^c, Prashant K. Jha^d, Chengyue Wu^{a,b,e,f,g}, John D. Hazle^b, Thomas E. Yankeelov^{a,b,h,i,j,k}, R Jason Stafford^b, Ahmed A. El-Gendy^l, David Fuentes^b

^a*Oden Institute for Computational Engineering and Sciences, The University of Texas at Austin, Austin, 78712, Texas, USA*

^b*Department of Imaging Physics, The University of Texas M.D. Anderson Cancer Center, Houston, 77030, Texas, USA*

^c*Applied Research Laboratories, The University of Texas at Austin, Austin, 78758, Texas, USA*

^d*Department of Mechanical Engineering, South Dakota School of Mines and Technology, Rapid City, 57701, South Dakota, USA*

^e*Department of Breast Imaging, The University of Texas M.D. Anderson Cancer Center, Houston, 77030, Texas, USA*

^f*Department of Biostatistics, The University of Texas M.D. Anderson Cancer Center, Houston, 77030, Texas, USA*

^g*The Institute for Data Science in Oncology, The University of Texas M.D. Anderson Cancer Center, Houston, 77030, Texas, USA*

^h*Department of Biomedical Engineering, The University of Texas at Austin, Austin, 78712, Texas, USA*

ⁱ*Department of Diagnostic Medicine, The University of Texas at Austin, Austin, 78712, Texas, USA*

^j*Department of Oncology, The University of Texas at Austin, Austin, 78712, Texas, USA*

^k*Livestrong Cancer Institutes, The University of Texas at Austin, Austin, 78712, Texas, USA*

^l*Department of Physics, University of Texas at El Paso, El Paso, 79968, Texas, USA*

Abstract

Magnetic nanoparticle hyperthermia is an emerging cancer therapy that utilizes magnetic nanoparticles subjected to alternating magnetic fields to generate localized heating and selectively target tumor tissues. Despite its potential, clinical implementation faces significant challenges due to uncertainties in the thermophysical properties, nanoparticle distribution, and magnetic particle parameters, which can compromise the precision and efficacy of the treatment. This article introduces an information-theoretic framework for optimal experimental design in magnetic nanoparticle hyperthermia to address these challenges. By accounting for uncertainties in key parameters, such as tissue thermal conductivity, blood perfusion rate, and nanoparticle anisotropy constant, the framework maximizes mutual information between the observed data and model parameters, enhancing the accuracy of parameter estimation. A surrogate 1D model is employed to reduce computational complexity, allowing the identification of optimal magnetic field amplitudes across diverse initial conditions and scenarios, including single and multiple uncertain parameters. The results highlight the robustness of the optimization approach, demonstrating consistent convergence to a stable solution that is expected to enable precise temperature measurement and effective parameter recovery. This study underscores the potential for mutual information-based optimization to advance the planning of magnetic nanoparticle hyperthermia treatment and provides a foundation for future experimental and clinical applications.

Keywords: Information-theory, mutual-information, magnetic hyperthermia, optimal

*Corresponding author

Email address: mahesh.nandyala@austin.utexas.edu (Mahesh Nandyala)

1. Introduction

Cancer is a global health problem and is rising and surpassing cardiovascular and cerebrovascular diseases as the leading cause of death [1]. To address this challenge, we need better and safer treatments. Traditional treatment methods, including surgery, chemotherapy, and radiation therapy, have limitations and side effects [2]. As a result, alternative or adjuvant treatments are being investigated to improve efficacy and minimize side effects. One such approach is hyperthermia therapy, which induces a therapeutic effect by raising the tissue temperature between 40 ° C and 45 ° C, thus killing or eradicating cancer cells [3]. Elevated temperature activates apoptotic pathways and makes cancer cells more susceptible to chemotherapy and radiation therapy [4, 5]. Recently, nanoparticle-based therapies, such as magnetic or photo-induced hyperthermia, are promising and minimally invasive options that offer targeted treatment [6]. Magnetic hyperthermia uses magnetic nanoparticles (MNPs) exposed to an alternating magnetic field (AMF) to generate localized heating within tumors, raise the temperature and damage malignant cells [7, 8, 9]. This method allows for precise targeting of tumors and less damage to surrounding healthy tissues, providing an advantage over the conventional methods [10]. A major advantage of magnetic hyperthermia is that it provides controlled and consistent heating and minimizes the risk of side effects [11]. FDA-approved superparamagnetic iron oxide nanoparticles as magnetic resonance imaging contrast agents accelerated the use of these particles in hyperthermia [12, 13, 14]. However, the clinical application of hyperthermia is hindered by several technical challenges, including uncertainties in tissue thermo-physical properties, variability in intratumoral nanoparticle distribution, particle-specific magnetic parameters, and differences in heat delivery methods among various hyperthermia treatments [15]. Enhancing the precision, safety, and effectiveness of magnetic nanoparticle hyperthermia requires a systematic approach to designing treatment parameters. This process involves adjusting key variables and conditions to achieve the most efficient and effective therapeutic outcomes. Within the context of magnetic nanoparticle hyperthermia, fine-tuning nanoparticle characteristics, improving intratumoral distribution, and optimizing magnetic field parameters are crucial for maximizing therapeutic efficacy while minimizing collateral damage to healthy tissues. By employing advanced optimization techniques, greater temperature control, improved heat localization within tumors, and consistent treatment outcomes can be achieved, making hyperthermia a more reliable and effective modality for cancer therapy. Systematic refinement of parameters ensures that treatment conditions are tailored to individual patient needs, reducing variability and enhancing clinical applicability. The following sections summarize previous research efforts focused on optimizing treatment parameters to advance the clinical potential of magnetic hyperthermia and highlight further research needed to improve the efficacy of treatment.

1.1. Prior work

Hyperthermia therapy has been studied for its ability to kill cancer cells directly and boost the effectiveness of chemotherapy and radiotherapy, making it an important adjuvant therapy in multi-modality cancer treatment [16, 17]. Preclinical and clinical trials in prostate cancer have shown better outcomes with hyperthermia [18, 19]. These efforts highlight that it can be both standalone and adjuvant therapy. Given this potential, many studies have focused on optimizing hyperthermia treatment protocols with regard to precision, safety, and efficacy. Jiang et al. [20] optimized nanoparticle delivery by studying multi-site magnetic nanoparticle injection using the Lattice Boltzmann method combined with particle swarm optimization. They found that increasing

the number of nanoparticle injection sites improved temperature homogeneity within the tumor, which is essential for uniform treatment and reducing the chance of overheating surrounding normal tissues. Wang et al. [21] developed an optimal temperature control system for tissues with gold nanoparticles using a two-energy equation model, which allows for precise temperature control by considering both conductive and convective heat transfer. Their approach minimized unintended thermal effects on surrounding tissues through periodic heating with an emphasis on controlled and localized treatment. Arora et al. [22] developed a minimum-time thermal dose control system that adjusted the treatment parameters to minimize the treatment time and prevent overheating of normal tissues. Their method was validated through simulations and in vitro experiments, showing the feasibility of time-optimal thermal therapy. They also explored the use of constrained predictive control in thermal therapies to optimize the treatment time while satisfying the safety constraints for normal tissues [23]. Barrera et al. [24] studied trapezoidal driving-field waveforms that improved specific loss power and temperature control and, hence, better cancer treatment. Abbasi and Malek [25] introduced a point-wise optimal control scheme based on the semigroup theory to refine heat delivery within tumor sites. By solving the thermal wave equation, they developed a strategy that controlled the heat deposition at the tumor location, optimizing the strength of the heat source while preventing damage to surrounding normal tissues. Although the above studies have advanced hyperthermia treatment by optimizing nanoparticle injection, temperature control, treatment efficacy, and safety for hyperthermia-based cancer therapy, the field has not systematically investigated patient-specific variability and uncertainties in thermophysical properties and nanoparticle distribution.

1.2. Gaps and motivation for this work

The effectiveness of magnetic nanoparticle hyperthermia is affected by various thermophysical properties, such as tissue density, specific heat, thermal conductivity, blood perfusion rate, and heat dissipation by particles. The efficiency of heat generation is also greatly affected by nanoparticle characteristics such as size, magnetic anisotropy constant, and magnetization strength. Conventional optimization methods in hyperthermia focus on enhancing thermal dose, typically measured through cumulative equivalent minutes at 43 ° C (CEM43) or thermal damage models, while assuming constant nanoparticle properties and tissue characteristics. These assumptions do not consider patient-specific variations, which may result in suboptimal or inconsistent treatment outcomes. We propose a model-based, information-theoretic approach to optimize experimental conditions, considering the uncertainty associated with the thermophysical properties of tissues and nanoparticle parameters during hyperthermia treatment. This approach accounts for both interpatient variability and inpatient heterogeneity across different organs, thereby improving the precision and reliability of hyperthermia therapy. Additionally, for newly synthesized nanoparticles designed for hyperthermia applications, important magnetic parameters are often unknown. In these situations, it is necessary to gather experimental data in order to fit suitable models and estimate these parameters. Randomized experimental designs could result in data that provide suboptimal information on the variables of interest, increasing the uncertainty in the recovered parameters and reducing the accuracy of parameter estimation. To address these challenges, we emphasize the importance of systematically designing and optimizing experiments to maximize the information obtained from temperature measurements. This study aims to identify an optimal magnetic field amplitude and its dynamic variation during treatment to improve parameter estimation accuracy, thereby improving the precision and effectiveness of hyperthermia therapy. By integrating information-theoretic optimization strategies, this framework aims to refine experimental protocols, minimize parameter uncertainty, and advance personalized magnetic hyperthermia treatment. Specifically, the parame-

ters considered for recovery or estimation in this study include tissue density, specific heat, thermal conductivity, blood perfusion rate, and the magnetic anisotropy constant. The information-theoretic framework introduced in this study is based on optimal experimental design methodologies, which leverage the Fisher information matrix and the Cramér-Rao bound to establish a lower limit on the variance of unbiased estimators [26, 27]. Indeed, the de Bruijn identity [28] offers a fundamental link between the derivatives of entropy calculations and the Fisher information matrix, reinforcing the theoretical foundation of this approach. Conventional approaches to optimizing the Fisher information matrix require prior estimates of tissue properties, such as density, specific heat, thermal conductivity, blood perfusion rate, and the particle magnetic anisotropy constant. These estimates are iteratively refined using experimental data, necessitating repeated optimization cycles. In contrast, the framework proposed in this study directly integrates parameter uncertainties by incorporating their probability distributions into mutual information (MI) calculations. This approach enables a more systematic and unified optimization of MI, eliminating the need for repeated re-optimization. By leveraging this novel framework, the study aims to enhance the accuracy of recovered parameters, ultimately improving treatment precision and efficacy in magnetic hyperthermia applications.

2. Methods

2.1. Heat transfer model

During thermal therapy-induced hyperthermia, the temperature of the tissue is elevated beyond the normal physiological temperature limit of 37 °C. Temperature distribution within the biological tissues is a complex process involving different aspects of heat transport including heat conduction within the tissues, blood perfusion and the associated convective transfer, heat generation due to tissue metabolic activity, and the local vasculature structure. Pennes [29] presented the first mathematical model for temperature distribution in biological tissues by analyzing heat transfer in a resting human forearm. Even though Pennes' bioheat equation (PBHE) was the first mathematical model (developed in 1948), it is still widely used in hyperthermia therapy modeling due to its simplicity. The PBHE describes the spatial-temporal distribution of temperature, $u(\mathbf{x}, t)$ at a given spatial location \mathbf{x} and time t within the biological tissue as:

$$\begin{aligned}
 \rho c \frac{\partial u}{\partial t} &= \nabla \cdot (k \nabla u) + \rho_b c_b \omega (u_b - u) + Q_m + Q_{\text{mnp}}(\mathbf{x}, t), \quad \forall \mathbf{x} \in \Omega, \\
 Q_{\text{mnp}}(\mathbf{x}, t) &= \alpha \times \text{SAR} \times C_{\text{mnp}}(\mathbf{x}), \\
 u(\mathbf{x}, 0) &= u_0(\mathbf{x}), \quad \mathbf{x} \in \Omega, \\
 \nabla u(\mathbf{x}, t) \cdot \mathbf{n} &= 0, \quad \mathbf{x} \in \partial\Omega_{\text{sym}}, \\
 -k \nabla u(\mathbf{x}, t) \cdot \mathbf{n} &= h(u - u_\infty), \quad \mathbf{x} \in \partial\Omega_{\text{conv}},
 \end{aligned} \tag{1}$$

where Ω is the domain volume, $\partial\Omega_{\text{sym}}$ is the symmetric boundary, $\partial\Omega_{\text{conv}}$ is the convective heat transfer boundary, ρ is the tissue density, c is the specific heat of the tissue, k is the tissue thermal conductivity, ρ_b is the blood density, c_b is the specific heat of the blood, ω is the blood perfusion rate in tissue, Q_m is the metabolic heat generation rate in the tissue, Q_{mnp} is the heat generated by the magnetic particles under the action of an external magnetic field, \mathbf{n} is the outward unit normal vector, h is the heat transfer coefficient, and u_∞ is the ambient air temperature. In this study, the metabolic heat generation rate is neglected, as the heat produced by MNPs significantly exceeds metabolic heat generation. The heat source due to the presence of nanoparticles, Q_{mnp} , is correlated to the magnetic nanoparticle concentration, C_{mnp} , and the specific absorption rate

(SAR) of the nanoparticles in aqueous solution, scaled by α to account for the crowded effects when particles are in tissues. The initial temperature of the tissue is denoted by $u_0(\mathbf{x})$, and Neumann and Robin boundary conditions are used appropriately on the domain boundaries. One of the main challenges in using the model given in Eq. (1) is that the tissue parameters are often unknown and can vary from one patient to another [30]. Therefore, it is reasonable to consider these parameters as uncertain, with some prior knowledge about their values.

2.2. Heat Generation by Magnetic Particles

Rosensweig [31] developed the theoretical background for understanding the heating mechanisms of magnetic nanoparticles when subjected to an external AMF. His approach was based on the Debye model for dielectric dispersion in polar fluids, under the assumption that magnetic nanoparticles exhibit a linear response to the applied magnetic field. Magnetic nanoparticles, under the action of an external AMF, generate heat due to Néel [32] and Brownian [33] relaxation mechanisms. When the magnetic fluid is exposed to an AMF, the nanoparticles in the fluid rotate to align the magnetic moments in the direction of the applied magnetic field. The two different ways to achieve this alignment are Brownian motion, in which the entire particle rotates in the liquid medium, and Néel relaxation, in which the magnetic moment within the particle rotates in the direction of the applied field. The Brownian (τ_B) and Néel (τ_N) relaxation times are expressed, respectively as follows:

$$\tau_B = \frac{3\mu V_H}{\kappa_B u_{ref}}, \quad (2)$$

and

$$\tau_N = \tau_0 \left(\frac{\sqrt{\pi}}{2} \right) \left(\sqrt{\frac{\kappa_B u_{ref}}{KV_M}} \right) \exp \left(\frac{KV_M}{\kappa_B u_{ref}} \right), \quad (3)$$

where μ is magnetic fluid viscosity, V_H is the hydrodynamic volume of the nanoparticle expressed as $V_H = \frac{4\pi(a+\delta)^3}{3}$, a is the particle radius, δ is the liquid layer thickness, κ_B is Boltzmann constant, u_{ref} is nanofluid temperature which is considered to be 37 °C (normal physiological temperature), τ_0 is the attempt time which represents the characteristic time scale associated with how frequently a magnetic moment attempts to switch its orientation due to thermal fluctuations and is considered to be 10^{-9} s for iron oxide nanoparticles [34], K is the magnetic anisotropy constant, and V_M is the magnetic volume of the particle expressed as $V_M = \frac{4\pi a^3}{3}$. Since both relaxation mechanisms contribute to heat dissipation, the overall relaxation behavior of the particles is characterized by the effective relaxation time (τ), which combines both Brownian and Néel contributions as:

$$\frac{1}{\tau} = \frac{1}{\tau_B} + \frac{1}{\tau_N}. \quad (4)$$

Under the influence of an AMF, magnetic nanoparticles undergo relaxation mechanisms that result in energy dissipation as heat. This thermal energy loss, governed by Néel and Brownian relaxation processes, is quantified as volumetric power dissipation (P), which defines the rate of heat generation per unit volume when nanoparticles are dispersed in a liquid medium. For a homogeneous and monodisperse suspension of magnetic nanoparticles, the volumetric power dissipation is given by:

$$P = \mu_0 \pi f H^2 \chi'', \quad (5)$$

where μ_0 is the magnetic permeability of free space, f is the frequency of the alternating field, H is the applied magnetic field amplitude, and χ'' is the loss/imaginary component of the magnetic susceptibility, which is expressed as:

$$\chi'' = \frac{2\pi f \tau}{1 + (2\pi f \tau)^2} \chi_0, \quad (6)$$

where τ is the effective relaxation time and χ_0 is the equilibrium (static) magnetic susceptibility which quantifies how much a material becomes magnetized when exposed to an external magnetic field. The static magnetic susceptibility (χ_0) is expressed as a function of initial magnetic susceptibility (χ_i) and Langevin parameters (ξ) as follows:

$$\chi_0 = \chi_i \frac{3}{\xi} \left(\cot(\xi) - \frac{1}{\xi} \right), \quad (7)$$

$$\chi_i = \frac{\mu_0 M_d^2 \phi V_M}{3 \kappa_B u_{ref}}, \quad (8)$$

$$\xi = \frac{\mu_0 M_d H V_M}{\kappa_B u_{ref}}, \quad (9)$$

where M_d is the domain magnetization of the magnetic particle. In general, the heating ability of the nanoparticles is expressed as the SAR representing the power generated per unit mass of the magnetic particle. The SAR of the nanoparticles is calculated from the volumetric heat dissipation by nanoparticles when dispersed in a liquid medium, which is expressed as:

$$\text{SAR} = \frac{P}{\rho_{\text{mnp}} \phi}, \quad (10)$$

where P is the volumetric power dissipation of the nanoparticles dispersed in the fluid, ρ_{mnp} is the mass density of the nanoparticles, and ϕ is the volume fraction of nanoparticles in the nanofluid.

2.3. Surrogate model

The first step in this investigation was the selection of the spatial domain and the corresponding model. The full 3D model consists of a spherical tumor embedded within a surrounding healthy skin layer, representing the computational domain. We calculated the complete 3D model solution in 9 minutes using the commercial software package COMSOL Multiphysics on a ten-core, 16 GB RAM, and 1.80 GHz laptop for 1800 s of treatment time. As the optimization procedure necessitates the computation of the forward model solution multiple times, a time-efficient solution strategy is required. Thus, we employed a one-dimensional surrogate model that maintains the geometric similarity to reduce the solution time during the optimization. The 1D model is based on the same governing equation as given in Eq.(1) and is geometrically the same as the 3D model. We then devised a numerical solution strategy using the backward Euler's method for time and a central differencing scheme for space. The computation time and temperature distribution predictions of the surrogate and full models are then compared. This approach proved to be highly efficient, with the computation time being 1.2 s for the surrogate model (compared to 9 minutes for the full 3D model) while providing an identical solution to the full model (details presented in the Results section). We refer to this 1D model as a surrogate model, and the 1D model replaces the original 3D model in the optimization step.

2.4. Mathematical Framework for Optimal Experimental Design

The parameters in the mathematical model, as described in Eqs. (1)–(10), that influence the temperature elevation are categorized into three groups: 1) Fixed (deterministic) parameters, which remain constant with known values, as listed in Table 1. 2) Model (uncertain) parameters, which vary between patients and nanoparticle systems. The model parameters $\mathcal{P} = \{\rho c, k, \omega, K\}$ are listed in Table 2. 3) Design parameters, defined as $\mathcal{K} = \{H_1, H_2, \dots, H_M\}$ where H_i represents the magnetic field amplitude over each time interval. As described in Eq. (5), the power deposition is

Table 1: List of fixed parameters in the model

Parameter	Value	Description
Computational domain (considered in this study)		
R_T	5 mm	Radius of the tumor
T_S	0.5 mm	Thickness of skin layer
Blood[35]		
ρ_b	1000 kg/m ³	Density
c_b	3840 J/kg·K	Specific heat
u_b	37 °C	Arterial blood temperature
Magnetic particle[36]		
d_{mnp}	16 nm	Particle diameter
δ	0.1 d_{mnp}	Liquid layer thickness
ρ_{mnp}	5180 kg/m ³	Particle density
M_d	446 kA/m	Magnetization
μ	1×10^{-3} Pa·s	Magnetic fluid viscosity
C_{mnp}	4 mg/cm ³ of tumor	MNP dose in tumor
V	1 ml	Injected magnetic nanofluid volume
Constant parameters[34, 37]		
μ_0	$4\pi \times 10^{-7}$ H/m	Permeability of free space
κ_B	1.34×10^{-23} J/K	Boltzmann constant
τ_0	1×10^{-9} s	Attempt time
α	0.55	Correction factor
Ambient parameters[38]		
h	10 W/m ² ·K	Heat transfer coefficient
u_∞	24 °C	Ambient temperature
Simulation parameters (considered in this study)		
f	163 kHz	Field frequency
t_f	1800 s	Treatment time
M	30	number of field on/off cycles (Time Steps)

Table 2: Model parameters (\mathcal{P}) used in initialization and optimization steps.

Parameter	Default value	Range	Description
ρc	3.5×10^6 kg/m ³	$[2.5 \times 10^6, 4.0 \times 10^6]$	Tissue density and specific heat product
k	0.492 W/mK	[0.300, 0.570]	Tissue thermal conductivity
ω	0.00682 1/s	[0.00111, 0.01390]	Blood perfusion rate
K	31500 J/m ³	[20000, 53000]	Magnetic anisotropy constant

directly proportional to the applied magnetic field H . During treatment, $H(t)$ is assumed to be piecewise constant over discrete time intervals Δt , leading to time-varying power dissipation. The magnetic field is therefore expressed as:

$$H(t) = \begin{cases} H_1 & t \in [0, \Delta t) \\ H_2 & t \in [\Delta t, 2\Delta t) \\ H_3 & t \in [2\Delta t, 3\Delta t) \\ \vdots & \\ H_M & t \in [(M-1)\Delta t, M\Delta t) \end{cases} \quad (11)$$

The goal of this work is to define and solve an optimization problem to determine the optimal design parameters $\mathcal{K} = \{H_1, H_2, \dots, H_M\}$, such that the uncertainty in the recovered thermophysical properties of the tumor and the magnetic anisotropy of the nanoparticle system is minimized based on available temperature measurements. To quantify the system response, we define the total signal $\mathcal{G}(\mathcal{K}, \mathcal{P}) \in \mathbb{R}$ from the physics-based model as the temperature field $u(t, x)$ integrated over the spatial domain Ω and time:

$$\mathcal{G}(\mathcal{K}, \mathcal{P}) = \int_{\Omega} \int_t u(t, x) dt d\Omega \quad (12)$$

The dependence of \mathcal{G} on both the design parameters \mathcal{K} and the model parameters \mathcal{P} arises from the coupled physics described in Eqs. (1)–(10). Note that this signal incorporates the full spatiotemporal evolution of the temperature field. In the optimization framework, we treat $\mathcal{G}(\mathcal{K}, \mathcal{P})$ as the observed data. Both the data and the model parameters $\mathcal{P} \equiv \{\rho c, k, \omega, K\}$ are considered as random variables. We then define the MI between the data and the model parameters and formulate an optimization problem to maximize the MI. This approach allows us to identify design parameters \mathcal{K} that maximize the information gained about the uncertain model parameters from temperature measurements.

Our data acquisition model, $\mathcal{G}(\mathcal{K}, \mathcal{P}) : \mathbb{R}^a \times \mathbb{R}^m \rightarrow \mathbb{R}^n$, maps deterministic acquisition parameters, $\mathcal{K} \in \mathbb{R}^a$, and uncertain parameters, $\mathcal{P} \in \mathbb{R}^m$ to observables, $\vec{z} \in \mathbb{R}^n$ (or $\vec{z} \in \mathbb{C}^n$). Explicitly, we will assume that the measurement models are corrupted by zero mean white noise of a known covariance matrix, $\Sigma_z \in \mathbb{R}^{n \times n}$

$$\vec{z} = \mathcal{G}(\mathcal{K}; \mathcal{P}) + \nu \quad \nu \sim \mathcal{N}(0, \Sigma_z), \quad (13)$$

where ν may be interpreted as the measurement noise or the acquisition noise in the sensor model. For a deterministic measurement model \mathcal{G} , the conditional probability distribution has an explicit analytical form and may be written as a known Gaussian distribution.

$$p(z|\mathcal{P}) = \mathcal{N}(\mathcal{G}(\mathcal{K}; \mathcal{P}), \Sigma_z) = \frac{1}{2\pi \det \Sigma_z} \exp\left(-\frac{1}{2}\|\mathcal{G}(\mathcal{K}; \mathcal{P}) - z\|_{\Sigma_z}^2\right), \quad (14)$$

Note that the noise, Σ_z , is a property of the measurement and is fixed and independent from the signal model $\mathcal{G}(\mathcal{K}; \mathcal{P})$. Additional known information is the prior probability distributions for the model parameters, $p(\mathcal{P})$. For simplicity, we assume that prior parameters are Gaussian distributed with known mean, $\hat{\mathcal{P}}$ and covariance, $\Sigma_{\mathcal{P}}$

$$\mathcal{P} \sim \mathcal{N}(\hat{\mathcal{P}}, \Sigma_{\mathcal{P}}) = \frac{1}{2\pi \det \Sigma_{\mathcal{P}}} \exp\left(-\frac{1}{2}\|\hat{\mathcal{P}} - \mathcal{P}\|_{\Sigma_{\mathcal{P}}}^2\right), \quad (15)$$

within this Bayesian setting, $\Sigma_{\mathcal{P}}$ represents the model parameter variation. Bayes's theorem is fundamental to the approach. The probability of the measurements $p(z)$ must be interpreted in

terms of the known information. The probability of the measurements may be derived from the marginalization of the joint probability and has the interpretation as the projection of the joint probability onto the measurement axis.

$$\begin{aligned}
p(z) &= \int_{\mathcal{P}} p(\mathcal{P}, z) d\mathcal{P} = \underbrace{\int_{\mathcal{P}} p(z|\mathcal{P}) p(\mathcal{P}) d\mathcal{P}}_{\int_{\rho_c} \int_{\kappa} \int_{\omega} \int_{\mathcal{K}}} \\
&= C \int_{\mathcal{P}} d\mathcal{P} \exp\left(-\frac{1}{2} \left(\|\mathcal{G}(\mathcal{K}; \mathcal{P}) - z\|_{\Sigma_z}^2 + \|\hat{\mathcal{P}} - \mathcal{P}\|_{\Sigma_{\mathcal{P}}}^2\right)\right),
\end{aligned} \tag{16}$$

2.4.1. MI calculation

We aim to identify measurement data that maximize the reliability of parameter estimates by significantly reducing uncertainty. According to information theory [28], this reduction is characterized by MI, which measures the amount of information gained about one variable through knowledge of another. MI has been extensively applied in various domains, such as image registration [39], optimizing sensor placement[40], sensor management [41], and parameter estimation [42]. We assume Gaussian distributions for the prior and likelihood, and the MI optimization reduces to entropy maximization.

$$\max_{\mathcal{K} \in \mathcal{F}} I(\mathcal{P}; z) = \max_{\mathcal{K} \in \mathcal{F}} H(z),$$

Calculating MI is a computationally intensive task due to the high-dimensional integration expressed in Eq. (17), needed across both parameter and data spaces. Various methods have been developed to perform these calculations, each demonstrating strengths that depend on the specific function involved. These methods encompass Monte Carlo and Quasi-Monte Carlo approaches[43, 44], lattice rules[45], adaptive subdivisions[46], neural network approximations[47], and numerical quadrature techniques[48]. In this work, Gauss-Hermite quadrature[49] is employed in each dimension of the MI integrals defined in Eq. (17) to perform numerical integration over multivariate Gaussian random variables (see Appendix [Appendix A](#)).

$$\begin{aligned}
H(z) &= - \int_z p(z) \ln p(z) dz \approx - \frac{1}{N_{out}} \sum_i^{N_{out}} \ln p(z_i), \\
&= - \int_z \int_{\mathcal{P}} \prod_i^N p(z_i|\mathcal{P}) p(\mathcal{P}) \ln \left(\int_{\hat{\mathcal{P}}} \prod_j^N p(\hat{\mathcal{P}}) p(z_j|\hat{\mathcal{P}}) d\hat{\mathcal{P}} \right) d\mathcal{P} dz, \\
p(z_i) &= \int_{\hat{\mathcal{P}}} p(\hat{\mathcal{P}}) p(z|\hat{\mathcal{P}}) d\hat{\mathcal{P}} \approx \frac{1}{N_{in}} \sum_j^{N_{in}} p(z_{i,j}|\hat{\mathcal{P}}_j),
\end{aligned} \tag{17}$$

where the \mathcal{P}_i are drawn from the prior $p(\mathcal{P})$; z_i are drawn from the conditional distribution $p(z_i|\mathcal{P}_i)$ (i.e., the likelihood), and N is the number of samples.

2.5. Monte Carlo integration of MI

Monte Carlo integration provides an independent numerical strategy to verify the results of experimental design optimization. The approach begins with the integral expression for the expectation of a function of a random variable. For a random variable X and a function $f(X)$, the expectation is given by $\mathbb{E}_X[f(X)] = \int_{\Omega_X} f(x) p_X(x) dx$ [43]. The entropy integral may thus be represented as an expectation, following this, the entropy can be written as $H(z) = \mathbb{E}_Z[\ln(p(z))]$. This will allow the use of Monte Carlo methods to approximate the integral numerically as $H(z) \approx \frac{-1}{N_{out}} \sum_i \ln(p(z_i))$,

where z_i are samples from the marginal distribution $p(z)$. However, it is not possible to directly calculate $p(z_i)$ because it is constructed as a marginal distribution, as in Eq. (16). To address this, we use a nested Monte Carlo for estimating $p(z_i)$ for given z_i . Using the Monte Carlo numerical decomposition, we can express $p(z_i)$ (i.e. the probability of some realization z_i) as the expectation integral $p(z_i) = \mathbb{E}_{\mathcal{P}}[p(z_0|\mathcal{P})]$. We can also estimate this quantity via a Monte Carlo method via sampling from $p_0(\mathcal{P})$ directly. This yields $p(z_i) = \int_{\mathcal{P}} p(z_i|\mathcal{P})p_0(\mathcal{P})d\mathcal{P} \approx \frac{1}{N_{in}} \sum_j p(z_0|p_j)$ with each p_j drawn from $p_0(\mathcal{P})$. The probability $p(z_0|\mathcal{P})$ is directly calculated from Eq. (14). Given this ability to evaluate $p(z_0)$ for individual realizations z_0 , the full differential entropy expression $H(z)$ is thus the average negative logarithm of the probabilities of realizations $p(z_i)$. The individual probabilities $p(z_i)$ are generated at the highest level, using a large number of realizations z_i from the distribution $p(z)$. Each realization z_i is generated first by sampling from $z_i \sim \int_{\mathcal{P}} p(z|\mathcal{P})p(\mathcal{P})d\mathcal{P}$. For realization z_i , we then use the Monte Carlo process described above, which involves the average of $p(z_i|p_j)$ with p_j according to samples from $p_0(\mathcal{P})$. The full Monte Carlo integration expression for the entropy is thus

$$H(z) = - \int_{\mathcal{Z}} p(z) \ln(p(z)) dz \approx \frac{-1}{N_{out}} \sum_i \ln \left(\frac{1}{N_{in}} \sum_j p(z_i|p_j) \right), \quad (18)$$

Importantly, N_{out} and N_{in} emerge as parameters required to control the convergence rate of the approximation. For known quantities, setting both to 10^3 yields an average error of approximately 5% for known mutual entropy calculations involving known \mathcal{K} . This is considered sufficient for benchmarking the performance of the integrations[50], and the results presented below assume these parameter settings.

3. Results

The concentric spherical geometry of the tumor and surrounding skin is depicted in Figure 1(a), providing a 3D representation of the spatial domain. The surrogate 1D model, shown in Figure 1(b), simplifies this geometry while maintaining geometric similarity and key thermal characteristics, thus enabling faster computations without compromising solution accuracy. This reduced dimensionality facilitates a more efficient optimization process by significantly reducing the requirements for computational resources. Figure 1(c) presents the temporal evolution of the the temperature at three critical locations: center of the tumor, the edge of the tumor and the surface of the skin. Solid lines represent the results of the 1D surrogate model, while markers illustrate the predictions of the 3D model. The close agreement between the surrogate model and the full 3D model demonstrates the surrogate's ability to capture the thermal behavior accurately. Specifically, the temperature curves from both models overlap at all time points, suggesting that the 1D surrogate model preserves essential features of heat transfer dynamics in the system. Figure 1(d) further compares the radial temperature profiles at multiple time points (0, 60, 120, and 1800 seconds). The results highlight the consistency between the predictions of the 1D and 3D models, with the surrogate model replicating the spatial temperature distribution observed in the full model. This indicates the surrogate model's ability to effectively approximate the spatial temperature distribution, at all treatment times and radial positions. The full 3D model required approximately nine minutes for a simulation spanning 1800 seconds, as computed using the COMSOL Multiphysics package, while the same simulation was completed in just 1.2 seconds using a simplified 1D model. The comparative results clearly illustrate that the surrogate 1D model is an efficient and accurate alternative to the computationally intensive 3D model. This makes the 1D surrogate model appealing for optimization procedures where repeated forward model evaluations are necessary. As described in section 2.4, multivariate Gaussian is taken as a prior for uncertain model parameters $\mathcal{P} = \{\rho c, k, \omega, K\}$, The

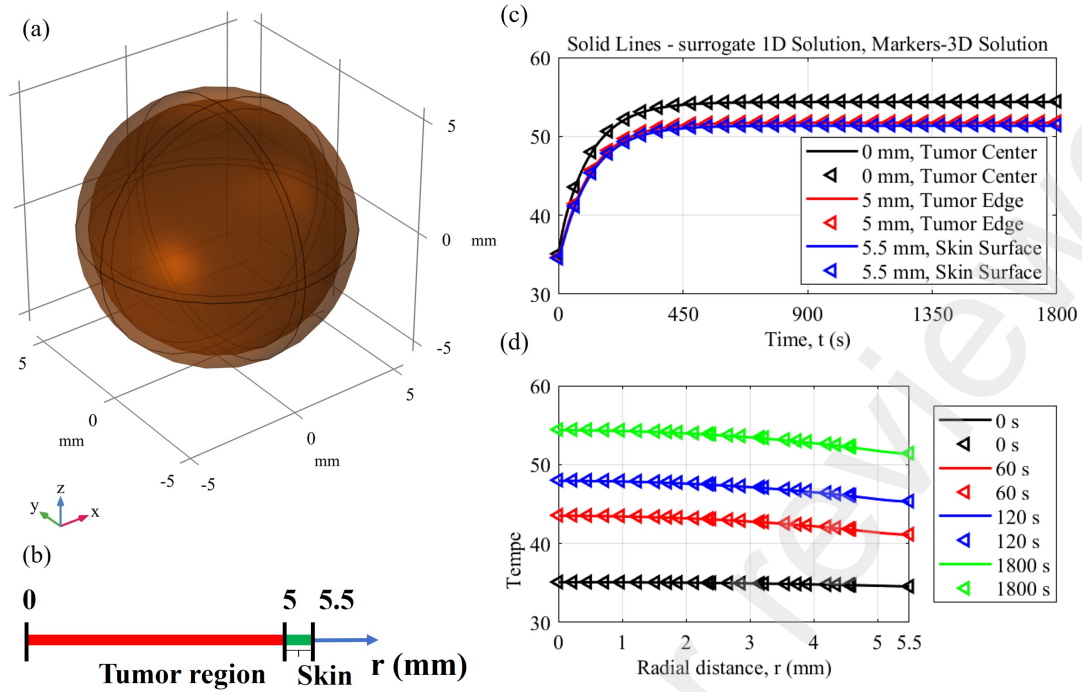


Figure 1: Computational Geometry and Comparison of Full and Surrogate Model Solutions. (a) The model consists of a three-dimensional concentric spherical geometry, where the tumor is surrounded by a skin layer, representing thermal behavior during treatment. (b) A one-dimensional surrogate model simplifies the 3D geometry, assuming symmetry at $r = 0$ and a convective boundary at the outer surface, ensuring computational efficiency while preserving thermal characteristics. (c) A comparison between the full 3D COMSOL model (markers) and the 1D MATLAB surrogate model (solid lines) shows strong agreement in temperature profiles at the tumor center, boundary, and outer surface, with steady-state reached after 600 seconds. (d) Radial temperature variation over time reveals progressive heating from MNPs, demonstrating the surrogate model's ability to capture key thermal dynamics while reducing computational complexity.

model parameters with the known mean and variance are as follows.

$$\text{Density and Specific Heat product: } \rho c = \mathcal{N}(3589229.92, 417740.68) \text{ J}/(\text{m}^3 \cdot \text{K})$$

$$\text{Thermal Conductivity: } k = \mathcal{N}(0.492, 0.076) \text{ W}/(\text{m} \cdot \text{K})$$

$$\text{Blood Perfusion Rate: } \omega = \mathcal{N}(0.00682, 0.00387) \text{ s}^{-1}$$

$$\text{Magnetic anisotropy constant: } K = \mathcal{N}(31500.00, 4725.00) \text{ J}/\text{m}^3$$

All quadrature points in the third-order Gauss-Hermite quadrature approximation for numerical integration were positive with the chosen mean and variance. The other model parameters were set as specified in Table 1. The bounds for the design variable \mathcal{K} were chosen to be $[0, 50,000]$ A/m. We have tried multiple initial guesses to arrive at the optimized value for \mathcal{K} . We have considered two cases for optimizing the design variable, as listed below.

1. *One uncertain parameter optimization.* In this case, the thermophysical properties of the tissue were assumed to be constant and fixed at the mean value. This results in the optimization problem of finding \mathcal{K} that minimizes the uncertainty in the magnetic anisotropy constant of the nanoparticles.
2. *Four uncertain parameters optimization.* In this case, all four model parameters are considered uncertain, and the optimization problem is to find \mathcal{K} with minimum uncertainty when these parameters are simultaneously recovered from the experimental measurements.

We initialized the optimization problem with fixed parameters for both cases and tested various initial guesses for the magnetic field amplitude (H) within the range of $[0, 40,000]$ A/m. The first six initial guesses were spaced evenly, with a step size of 8,000 A/m. Additionally, we explored two more cases: one with a randomly varying H and another with an oscillating H between 0 and 7,600 A/m, as described in [51]. These diverse initial conditions were used to evaluate the robustness of the optimization algorithm in converging to optimal solutions. Figure 2 and Figure 3 illustrate the results of an optimization problem designed to determine the optimal values of \mathcal{K} for cases 1 and 2, respectively. In Figure 2, results from Case 1 are presented, where only the magnetic anisotropy constant (K) is treated as an uncertain parameter. The optimization algorithm aimed to maximize the MI between the data $\mathcal{G}(\mathcal{K}, \mathcal{P})$ and the model parameters \mathcal{P} . The optimizer consistently converges to stable and positive magnetic field amplitudes (H) near the maximum allowable value for all nonzero initial guesses. This demonstrates the robustness and efficiency of the optimization process in refining initial guesses to achieve optimal solutions. However, the optimizer fails to identify and refine a solution when the initial guesses are set to zero, as shown in panel a, and for nonzero initial guesses in d and f. This failure suggests that the algorithm requires nonzero starting points to initiate the optimization process effectively. Interestingly, when the nonzero initial guesses are slightly perturbed by a small fluctuation of 10 A/m, the optimizer can refine these values and successfully converge to the optimal magnetic field amplitudes identical to the observed values in panels b, c, and e, where the optimization consistently achieves stable and maximum amplitude solutions. These findings highlight the importance of appropriate initial conditions and the sensitivity of the optimization process to minor perturbations in the input values. In Figure 3, the results for Case 2, where all model parameters are treated as uncertain parameters, illustrate the optimization framework’s ability to handle increased complexity and uncertainty. Sub-panels (a)-(f) show the algorithm’s effectiveness in refining evenly spaced initial guesses, consistently converging to stable solutions near the maximum allowable field amplitude for all nonzero initial guesses. Sub-panel (g) highlights the framework’s robustness in dealing with randomly varying magnetic field amplitudes, successfully converging to consistent optimized values. Similarly, sub-panel (h) demonstrates the algorithm’s adaptability to oscillatory inputs, effectively refining these complex initial conditions to achieve optimal solutions. These results confirm the framework’s ability to address diverse scenarios, enabling the design of robust experimental protocols under conditions of high uncertainty.

The optimal values obtained using the quadrature integration method are verified through Monte Carlo integration, as illustrated in Figure 4. The figure presents the distribution of cost function values computed for 500 samples using both random and optimal design parameters. A clear separation is observed between the cost values corresponding to the random and optimal parameters for both the one and four uncertain parameter cases. Notably, the cost function values are consistently higher for the optimal parameters, indicating higher entropy. These results confirm the correctness of the optimal parameters identified through the information-theoretic optimization based on quadrature integration.

4. Discussion

The results demonstrate the effectiveness of the proposed optimization framework in determining optimal design parameters \mathcal{K} for reducing uncertainty in model parameters. The convergence to stable and positive optimized values for widely varying initial guesses indicates that the MI framework is robust and reliable for optimization problems. This suggests that the optimization algorithm is well suited for simplifying the design process with uncertain model parameters. In

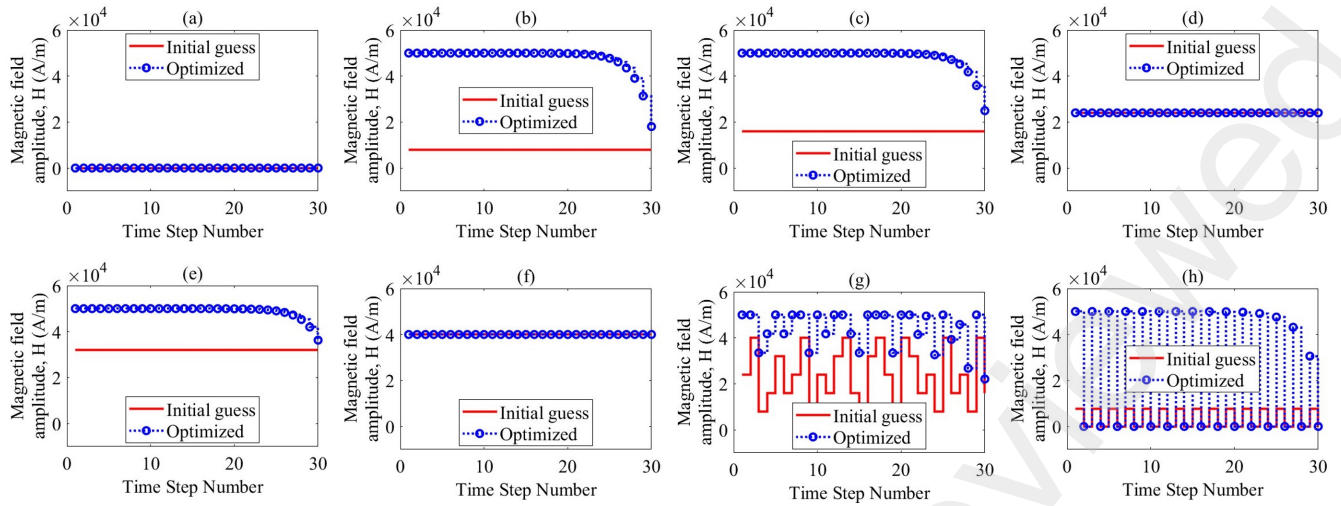


Figure 2: Optimization results for Case 1, where only K is treated as a random variable. The plots compare the initial guesses (red solid lines) with the optimized magnetic field amplitudes (H , blue circles) across various scenarios. The initial guesses include evenly spaced values (0,8,000,...,40,000 A/m) (sub-panels a-f), a randomly varying H (g), and an oscillating H between 0 and 7,600 A/m (h). The optimizer consistently converges to stable and positive H values near the maximum allowable amplitude for all nonzero initial guesses. However, the optimizer fails to refine the solution for initial guesses in panels a, d, and f. When these values are perturbed by a small fluctuation of 10 A/m, the optimizer successfully converges to optimal values, similar to the results observed in panels b, c, and e.

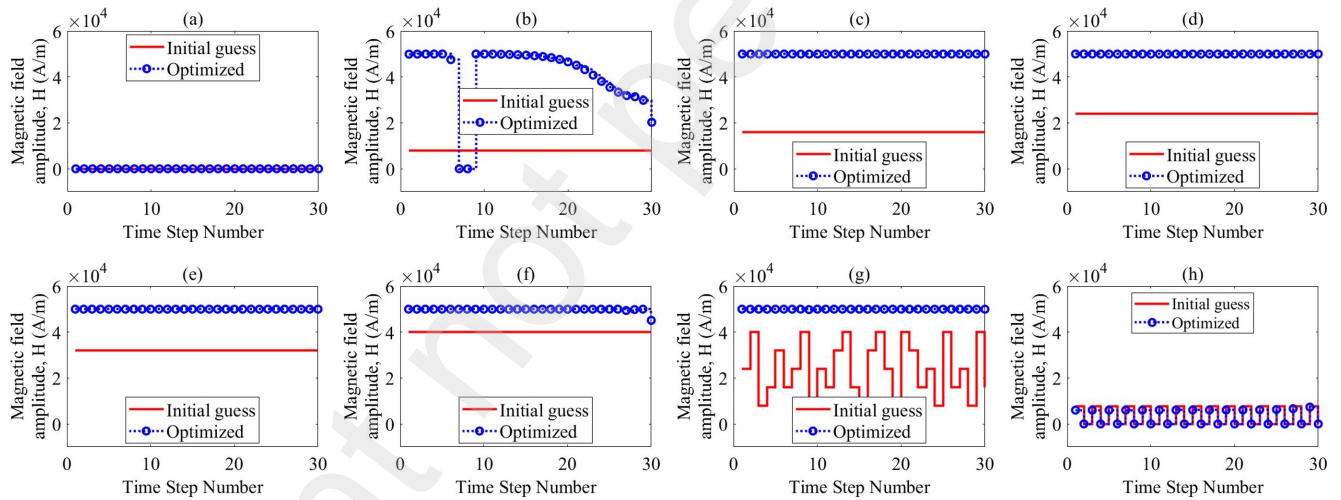


Figure 3: Optimization results for Case 2, where all model parameters are treated as random variables. The plots compare initial guess (red solid lines) with optimized magnetic field amplitudes (H , blue circles) for evenly spaced values (0,8,000,...,40,000 A/m) (sub-panels a-f), a randomly varying H (g), and an oscillating H between 0 and 7,600 A/m (h). The optimizer refined the solutions and found optimal values other than the given initial condition for all the initial guesses except a zero initial guess.

most cases, the clear difference between initial guesses and optimized values highlights the ability of a MI-based approach to guide the optimization process. By leveraging MI, the model ensures that the design parameters provide maximal information about the uncertain parameters, enabling more accurate and reliable parameter estimation from temperature measurements. The application of MI theory to identify optimal experimental parameters has been validated in our previous studies [49, 52, 53]. For example, Jha et al. [49] demonstrated computationally how information

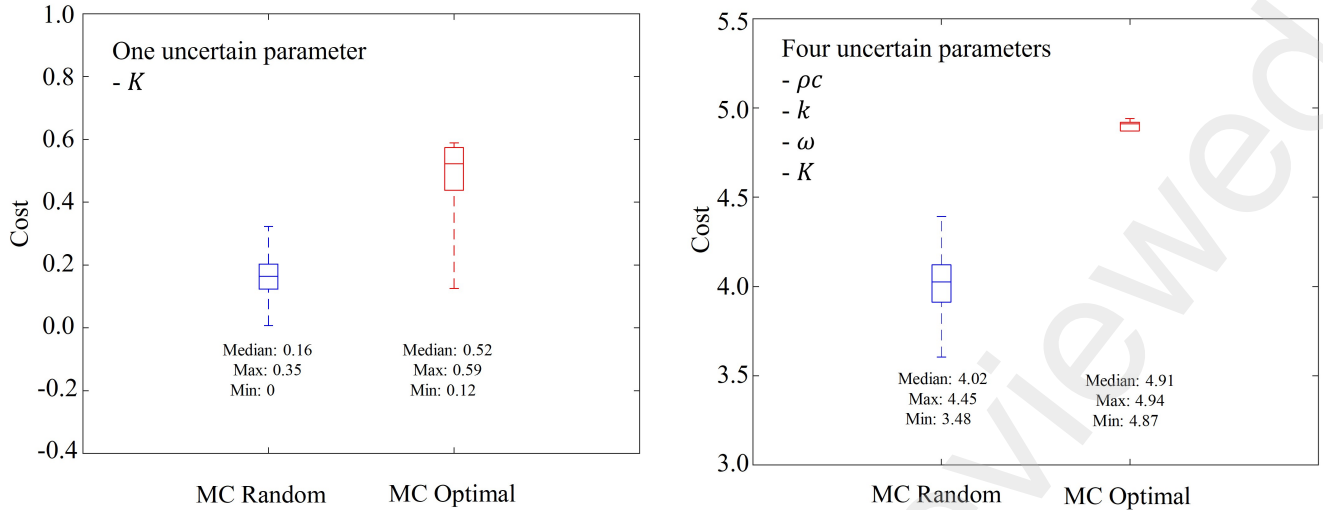


Figure 4: We plot the difference in cost function between random and optimal points using box plots. The left panel demonstrates the distribution of values for the MI for one uncertain parameter, while the right panel demonstrates four uncertain variables. Both sets of plots are the cost function associated with $H(z|\mathcal{K})$. The blue plots are the cost distribution for 500 random experimental parameter realizations, uniformly distributed and computed via the Monte Carlo integration technique. The red plots are the distribution of optimal cost values at the optimally computed points. The separation between random and optimal costs helps verify the utility of the optimization, and the independent calculation method further verifies the main result.

theory-based optimization could effectively identify image acquisition parameters for recovering the pyruvate-to-lactate exchange rate. Similarly, Madankan et al. [52] validated the use of MI for selecting optimal k-space locations in MRI, using phantom acquisitions as proof of concept. Mitchell et al. [53] extended this work by optimizing MRI acquisition parameters for 3D quantification with an interleaved Look-Locker sequence (3D-QALAS), validated using both mathematical phantoms and in-vivo human brain imaging. These studies collectively highlight the robustness and versatility of information theory-based approaches in optimizing experimental conditions across a wide range of applications. Based on this established foundation, we did not explicitly validate our optimized parameters in this study with the experiments. However, we used Monte Carlo integration techniques to verify our results, which strongly support the validity of our approach. Future work will involve validating the framework through both experimental and computational approaches, including in-vivo and in-silico studies. Planned in-vivo experiments will utilize mouse models with breast and prostate cancer cell lines to conduct hyperthermia treatments. During these experiments, temperature measurements will be taken under both random and optimized magnetic field conditions. The recorded temperature data, reflecting uncertainties in model parameters, will serve as the observed dataset. By integrating the model with the measured temperature data, the parameters of interest will be recovered, and the associated uncertainties will be systematically evaluated. Additionally, a computational validation approach will be employed, where synthetic data, such as temperature profiles, will be generated using the model under controlled noise conditions. This synthetic data will then be used to evaluate the recovery accuracy of the parameters of interest. These efforts will comprehensively test the framework’s efficacy and pave the way for real-world applications. A limitation of this study is the theoretical nature of the data acquisition model coming from the solution of PBHE. However, the bioheat transfer model and the magnetic particle heat generation theory have been widely used in various studies [36, 38, 54, 55] to model magnetic nanoparticle

hyperthermia. These studies strongly agreed with the experimental data when parameterized with physically realistic values. Therefore, the findings presented in this work can provide valuable insights for designing and optimizing future experiments. This work uses a Gaussian prior to handle the uncertainty in thermophysical tissue characteristics and the anisotropic energy constant of nanoparticles. The study may produce a more reliable evaluation of the stability of the findings using more uncertain parameters. Furthermore, investigating different prior distributions, such as uniform priors, could offer new perspectives. The computational architecture used in this study relies on a quadrature method to evaluate MI integrals, which have intrinsic constraints. Adding extra sources of uncertainty poses issues due to the "curse of dimensionality". To overcome this issue, alternate integration approaches, such as Markov Chain Monte Carlo or nested sampling methods for evaluating MI integrals, may provide more efficiency and scalability.

5. Conclusions

This study presents an information-theoretic framework for optimizing experimental conditions in magnetic nanoparticle hyperthermia, addressing key challenges associated with uncertainties in the thermophysical properties, nanoparticle distribution, and magnetic parameters. By incorporating mutual information as a metric during the proposed optimization approach, this study optimized the magnetic field amplitude for better temperature measurements to improve the accuracy of parameter estimation. The results demonstrate the robustness of the optimization process in diverse initial guesses, with consistent convergence to stable and meaningful solutions, even in scenarios with multiple uncertain parameters. This framework provides a powerful tool for improving the planning of magnetic nanoparticle hyperthermia treatment and highlights the potential of its integration into clinical workflows to enhance the safety, efficacy, and predictability of hyperthermia-based cancer therapies. Future work should focus on experimental validation and extend this approach to more complex 3D geometries and real-time treatment monitoring.

Ethics Statement

This study did not involve human participants, animals, or any data requiring ethical approval.

CRedit authorship contribution statement

Mahesh Nandyala: Conceptualization, Methodology, Software, Formal analysis, Visualization, Writing – Original Draft. **Andrew Lanham:** Software, Validation, Visualization, Writing – Original Draft. **Prashant K. Jha:** Software, Writing – Review & Editing. **Chengyue Wu:** Writing – Review & Editing. **John D. Hazle:** Supervision, Writing – Review & Editing. **Thomas E. Yankeelov:** Supervision, Writing – Review & Editing. **R Jason Stafford:** Conceptualization, Supervision, Writing – Review & Editing. **Ahmed A. El-Gendy:** Conceptualization, Writing – Review & Editing. **David Fuentes:** Conceptualization, Methodology, Software, Writing – Review & Editing, Supervision.

Declaration of competing interest

The authors declare that they have no known competing financial interests or personal relationships that could have appeared to influence the work reported in this paper.

Acknowledgements

The authors R Jason Stafford and Ahmed A. El-Gendy acknowledge the support from the Cancer Prevention and Research Institute of Texas (CPRIT) with grant #RP210153.

Appendix

Appendix A. Gauss Hermite Quadrature

1D Gauss-Hermite quadrature is of the form:

$$\int_{-\infty}^{\infty} \exp(-x^2) f(x) dx \approx \sum_i \omega_i f(x_i), \quad \omega_i = \dots \quad (\text{A1})$$

Consider $p(z)$:

$$p(z) = \int_{\hat{p}_1} \int_{\hat{p}_2} \int_{\hat{p}_N} \prod_j^N p(\hat{p}_j) p(z|\hat{p}) d\hat{p} = \int_{\hat{p}_1} p(\hat{p}_1) \int_{\hat{p}_2} p(\hat{p}_2) \int_{\hat{p}_N} p(\hat{p}_N) p(z|\hat{p}) d\hat{p} \quad (\text{A2})$$

We can consider several probability models. First, consider a conditional probability model where each time point and species is jointly independent:

$$\begin{aligned} p(z|\mathcal{P}) &= p(z_1|\mathcal{P})p(z_2|\mathcal{P}) \dots p(z_n|\mathcal{P}) \\ &= \mathcal{N}(\mathcal{G}_1(\mathcal{K}; \mathcal{P}), \sigma_z) \mathcal{N}(\mathcal{G}_2(\mathcal{K}; \mathcal{P}), \sigma_z) \dots \mathcal{N}(\mathcal{G}_n(\mathcal{K}; \mathcal{P}), \sigma_z) \\ &= \prod_{i=1}^n \frac{1}{\sqrt{2\pi}\sigma_z} \exp\left(-\frac{1}{2} \left(\frac{\mathcal{G}_i(\mathcal{K}; \mathcal{P}) - z_i}{\sigma_z}\right)^2\right) \\ &= \frac{1}{(\sqrt{2\pi}\sigma_z)^n} \exp\left(-\frac{1}{2\sigma_z^2} \|\vec{\mathcal{G}}(\mathcal{K}; \mathcal{P}) - \vec{z}\|_2^2\right). \end{aligned} \quad (\text{A3})$$

Alternatively, we can consider the signal total sum as a scalar Gaussian variable:

$$p(z|\mathcal{P}) = \mathcal{N}(\mathcal{G}(\mathcal{K}; \mathcal{P}), \sigma_z) = \frac{1}{\sqrt{2\pi}\sigma_z} \exp\left(-\frac{1}{2} \left(\frac{\mathcal{G}(\mathcal{K}; \mathcal{P}) - z}{\sigma_z}\right)^2\right) \quad (\text{A4})$$

$$\mathcal{P} \sim \mathcal{N}(\hat{\mathcal{P}}, \Sigma_{\mathcal{P}}) = \prod_{i=1}^N \frac{1}{\sqrt{2\pi}\sigma_{\mathcal{P}_i}} \exp\left(-\frac{1}{2} \left(\frac{\mu_{\mathcal{P}_i} - \mathcal{P}_i}{\sigma_{\mathcal{P}_i}}\right)^2\right) \quad (\text{A5})$$

For each component:

$$\begin{aligned} \int_{\mathcal{P}_i} p(\mathcal{P}_i) p(z|\mathcal{P}_1, \mathcal{P}_2, \mathcal{P}_i, \mathcal{P}_N) d\mathcal{P}_i &= \int_{\mathcal{P}_i} \frac{1}{\sqrt{2\pi}\sigma_{\mathcal{P}_i}} \exp\left(-\frac{1}{2} \left(\frac{\mathcal{P}_i - \mu_{\mathcal{P}_i}}{\sigma_{\mathcal{P}_i}}\right)^2\right) \\ &\quad \times p(z|\mathcal{P}_1, \mathcal{P}_2, \mathcal{P}_i, \mathcal{P}_N) d\mathcal{P}_i \\ &= \int_x \frac{1}{\sqrt{2\pi}\sigma_{\mathcal{P}_i}} \exp(-x^2) p(z|\mathcal{P}_1, \mathcal{P}_2, \sqrt{2}\sigma_{\mathcal{P}_i}x + \mu_{\mathcal{P}_i}, \mathcal{P}_N) \\ &\quad \times \sqrt{2}\sigma_{\mathcal{P}_i} dx \\ &= \int_x \frac{1}{\sqrt{\pi}} \exp(-x^2) p(z|\mathcal{P}_1, \mathcal{P}_2, \sqrt{2}\sigma_{\mathcal{P}_i}x + \mu_{\mathcal{P}_i}, \mathcal{P}_N) dx \\ &\approx \sum_j \omega_j \frac{1}{\sqrt{\pi}} p(z|\mathcal{P}_1, \mathcal{P}_2, \sqrt{2}\sigma_{\mathcal{P}_i}x_j + \mu_{\mathcal{P}_i}, \mathcal{P}_N) \end{aligned} \quad (\text{A6})$$

Here, a change of variables is assumed:

$$x = \frac{\mathcal{P}_i - \mu_{\mathcal{P}_i}}{\sqrt{2}\sigma_{\mathcal{P}_i}}, \quad \mathcal{P}_i = \sqrt{2}\sigma_{\mathcal{P}_i}x + \mu_{\mathcal{P}_i}, \quad d\mathcal{P}_i = \sqrt{2}\sigma_{\mathcal{P}_i}dx \quad (\text{A7})$$

Continuing to the next variable:

$$\begin{aligned} & \int_{\mathcal{P}_k} p(\mathcal{P}_k) \sum_j \omega_j \frac{1}{\sqrt{\pi}} p(z|\mathcal{P}_1, \mathcal{P}_k, \sqrt{2}\sigma_{\mathcal{P}_i}x_j + \mu_{\mathcal{P}_i}, \mathcal{P}_N) d\mathcal{P}_k \\ & \approx \sum_l \omega_l \sum_j \omega_j \frac{1}{\sqrt{\pi}} \times p\left(z|\mathcal{P}_1, \sqrt{2}\sigma_{\mathcal{P}_k}x_l + \mu_{\mathcal{P}_k}, \sqrt{2}\sigma_{\mathcal{P}_i}x_j + \mu_{\mathcal{P}_i}, \mathcal{P}_N\right) \end{aligned} \quad (\text{A8})$$

By induction:

$$p(z) \approx \sum_{j_N} \omega_{j_N} \sum_{j_2} \omega_{j_2} \sum_{j_1} \omega_{j_1} \frac{1}{\sqrt{\pi}^N} p\left(z|\sqrt{2}\sigma_{\mathcal{P}_1}x_{j_1} + \mu_{\mathcal{P}_1}, \sqrt{2}\sigma_{\mathcal{P}_2}x_{j_2} + \mu_{\mathcal{P}_2}, \sqrt{2}\sigma_{\mathcal{P}_N}x_{j_N} + \mu_{\mathcal{P}_N}\right) \quad (\text{A9})$$

Notice that the $p(z)$ calculation is independent of whether the conditional probability $p(z|\mathcal{P})$ is Gaussian or Rician. The parameter prior $p(\mathcal{P})$ is Gaussian in either case. Integration is with respect to the parameter prior. Integration is linear:

$$\int af(x) + bg(x) + ch(x)dx = a \int f(x)dx + b \int g(x)dx + c \int h(x)dx \quad (\text{A10})$$

References

- [1] K. ReFaey, S. Tripathi, S. S. Grewal, A. G. Bhargav, D. J. Quinones, K. L. Chaichana, S. O. Antwi, L. T. Cooper, F. B. Meyer, R. S. Dronca, R. B. Diasio, and A. Quinones-Hinojosa, "Cancer mortality rates increasing vs cardiovascular disease mortality decreasing in the world: Future implications," *Mayo Clin. Proc. Innov. Qual. Outcomes*, vol. 5, no. 3, pp. 645–653, 2021. [Online]. Available: <https://doi.org/10.1016/j.mayocpiqo.2021.05.005>
- [2] P. K. Jain, I. H. El-Sayed, and M. A. El-Sayed, "Au nanoparticles target cancer," *Nano Today*, vol. 2, no. 1, pp. 18–29, 2007. [Online]. Available: [https://doi.org/10.1016/S1748-0132\(07\)70016-6](https://doi.org/10.1016/S1748-0132(07)70016-6)
- [3] X. Liu, Y. Zhang, Y. Wang, W. Zhu, G. Li, X. Ma, Y. Zhang, S. Chen, S. Tiwari, K. Shi, S. Zhang, H. M. Fan, Y. Zhao, and X.-J. Liang, "Comprehensive understanding of magnetic hyperthermia for improving antitumor therapeutic efficacy," *Theranostics*, vol. 10, no. 8, pp. 3793–3815, 2020. [Online]. Available: <https://doi.org/10.7150/thno.40805>
- [4] M. Johannsen, B. Thiesen, U. Gneveckow, K. Taymoorian, N. Waldöfner, R. Scholz, S. Deger, K. Jung, S. A. Loening, and A. Jordan, "Thermotherapy using magnetic nanoparticles combined with external radiation in an orthotopic rat model of prostate cancer," *Prostate*, vol. 66, no. 1, pp. 97–104, 2006. [Online]. Available: <https://doi.org/10.1002/pros.20324>
- [5] J. van der Zee and M. C. C. M. Hulshof, "Lessons learned from hyperthermia," *Int. J. Radiat. Oncol. Biol. Phys.*, vol. 57, no. 2, pp. 596–597, 2003. [Online]. Available: [https://doi.org/10.1016/S0360-3016\(03\)00419-X](https://doi.org/10.1016/S0360-3016(03)00419-X)

- [6] S. K. Sharma, N. Shrivastava, F. Rossi, L. D. Tung, and N. T. K. Thanh, “Nanoparticles-based magnetic and photo-induced hyperthermia for cancer treatment,” *Nano Today*, vol. 29, p. 100795, 2019. [Online]. Available: <https://doi.org/10.1016/j.nantod.2019.100795>
- [7] J. Jose, R. Kumar, S. Harilal, G. E. Mathew, D. G. T. Parambi, A. Prabhu, M. S. Uddin, L. Aleya, H. Kim, and B. Mathew, “Magnetic nanoparticles for hyperthermia in cancer treatment: an emerging tool,” *Environ. Sci. Pollut. Res.*, vol. 27, no. 16, pp. 19 214–19 225, 2020. [Online]. Available: <https://doi.org/10.1007/s11356-019-07231-2>
- [8] C. L. Dennis and R. Ivkov, “Physics of heat generation using magnetic nanoparticles for hyperthermia,” *Int. J. Hyperthermia*, vol. 29, no. 8, pp. 715–729, 2013. [Online]. Available: <https://doi.org/10.3109/02656736.2013.836758>
- [9] K. Ahmed, Y. Tabuchi, and T. Kondo, “Hyperthermia: an effective strategy to induce apoptosis in cancer cells,” *Apoptosis*, vol. 20, no. 11, pp. 1411–1419, 2015. [Online]. Available: <https://doi.org/10.1007/s10495-015-1168-3>
- [10] V. Vilas-Boas, F. Carvalho, and B. Espiña, “Magnetic hyperthermia for cancer treatment: Main parameters affecting the outcome of in vitro and in vivo studies,” *Molecules*, vol. 25, no. 12, p. 2874, 2020. [Online]. Available: <https://doi.org/10.3390/molecules25122874>
- [11] A. Andreozzi, L. Brunese, M. Iasiello, C. Tucci, and G. P. Vanoli, “Modeling heat transfer in tumors: A review of thermal therapies,” *Ann. Biomed. Eng.*, vol. 47, no. 3, pp. 676–693, 2019. [Online]. Available: <https://doi.org/10.1007/s10439-018-02177-x>
- [12] L. H. Reddy, J. L. Arias, J. Nicolas, and P. Couvreur, “Magnetic nanoparticles: Design and characterization, toxicity and biocompatibility, pharmaceutical and biomedical applications,” *Chem. Rev.*, vol. 112, no. 11, pp. 5818–5878, 2012. [Online]. Available: <https://doi.org/10.1021/cr300068p>
- [13] P. Das, M. Colombo, and D. Prospero, “Recent advances in magnetic fluid hyperthermia for cancer therapy,” *Colloids Surf. B Biointerfaces*, vol. 174, pp. 42–55, 2019. [Online]. Available: <https://doi.org/10.1016/j.colsurfb.2018.10.051>
- [14] C. S. S. R. Kumar and F. Mohammad, “Magnetic nanomaterials for hyperthermia-based therapy and controlled drug delivery,” *Adv. Drug Deliv. Rev.*, vol. 63, no. 9, pp. 789–808, 2011. [Online]. Available: <https://doi.org/10.1016/j.addr.2011.03.008>
- [15] M. Bañobre-López, A. Teijeiro, and J. Rivas, “Magnetic nanoparticle-based hyperthermia for cancer treatment,” *Rep. Pract. Oncol. Radiother.*, vol. 18, no. 6, pp. 397–400, 2013. [Online]. Available: <https://doi.org/10.1016/j.rpor.2013.09.011>
- [16] R. D. Issels, L. H. Lindner, J. Verweij, P. Wust, P. Reichardt, B.-C. Schem, S. Abdel-Rahman, S. Daugaard, C. Salat, C.-M. Wendtner, Z. Vujaskovic, R. Wessalowski, K.-W. Jauch, H. R. Dürr, F. Ploner, A. Baur-Melnyk, U. Mansmann, W. Hiddemann, J.-Y. Blay, and P. Hohenberger, “Neo-adjuvant chemotherapy alone or with regional hyperthermia for localised high-risk soft-tissue sarcoma: a randomised phase 3 multicentre study,” *Lancet Oncol.*, vol. 11, no. 6, pp. 561–570, 2010. [Online]. Available: [https://doi.org/10.1016/S1470-2045\(10\)70071-1](https://doi.org/10.1016/S1470-2045(10)70071-1)
- [17] T. S. Herman and B. A. Teicher, “Summary of studies adding systemic chemotherapy to local hyperthermia and radiation,” *Int. J. Hyperthermia*, vol. 10, no. 3, pp. 443–449, 1994. [Online]. Available: <https://doi.org/10.3109/02656739409010290>

- [18] M. Johannsen, B. Thiesen, P. Wust, and A. Jordan, “Magnetic nanoparticle hyperthermia for prostate cancer,” *Int. J. Hyperthermia*, vol. 26, no. 8, pp. 790–795, 2010. [Online]. Available: <https://doi.org/10.3109/02656731003745740>
- [19] M. Johannsen, U. Gneveckow, L. Eckelt, A. Feussner, N. Waldöfner, R. Scholz, S. Deger, P. Wust, S. A. Loening, and A. Jordan, “Clinical hyperthermia of prostate cancer using magnetic nanoparticles: presentation of a new interstitial technique,” *Int. J. Hyperthermia*, vol. 21, no. 7, pp. 637–647, 2005. [Online]. Available: <https://doi.org/10.1080/02656730500158360>
- [20] Q. Jiang, F. Ren, C. Wang, Z. Wang, G. Kefayati, S. Kenjeres, K. Vafai, Y. Liu, and H. Tang, “On the magnetic nanoparticle injection strategy for hyperthermia treatment,” *Int. J. Mech. Sci.*, vol. 235, p. 107707, 2022. [Online]. Available: <https://doi.org/10.1016/j.ijmecsci.2022.107707>
- [21] S.-L. Wang, H. Qi, Y.-T. Ren, Q. Chen, and L.-M. Ruan, “Optimal temperature control of tissue embedded with gold nanoparticles for enhanced thermal therapy based on two-energy equation model,” *J. Therm. Biol.*, vol. 74, pp. 264–274, 2018. [Online]. Available: <https://doi.org/10.1016/j.jtherbio.2018.04.011>
- [22] D. Arora, M. Skliar, and R. B. Roemer, “Minimum-time thermal dose control of thermal therapies,” *IEEE Trans. Biomed. Eng.*, vol. 52, no. 2, pp. 191–200, 2005. [Online]. Available: <https://doi.org/10.1109/TBME.2004.840471>
- [23] D. Arora, M. Skliar, D. Cooley, and R. B. Roemer, “Constrained predictive control of thermal therapies for minimum-time delivery of thermal dose,” *IEEE Trans. Control Syst. Technol.*, vol. 15, no. 6, pp. 1030–1037, 2007. [Online]. Available: <https://doi.org/10.1109/TCST.2007.899680>
- [24] G. Barrera, P. Allia, and P. Tiberto, “Fine tuning and optimization of magnetic hyperthermia treatments using versatile trapezoidal driving-field waveforms,” *Nanoscale Adv.*, vol. 2, no. 9, pp. 3858–3867, 2020. [Online]. Available: <https://doi.org/10.1039/D0NA00358A>
- [25] G. Abbasi and A. Malek, “Pointwise optimal control for cancer treatment by hyperthermia with thermal wave bioheat transfer,” *Automatica*, vol. 111, p. 108579, 2020. [Online]. Available: <https://doi.org/10.1016/j.automatica.2019.108579>
- [26] O. Brihuega-Moreno, F. P. Heese, and L. D. Hall, “Optimization of diffusion measurements using cramer-rao lower bound theory and its application to articular cartilage,” *Magn. Reson. Med.*, vol. 50, no. 5, pp. 1069–1076, 2003. [Online]. Available: <https://doi.org/10.1002/mrm.10628>
- [27] S. J. Reeves and Z. Zhao, “Sequential algorithms for observation selection,” *IEEE Trans. Signal Process.*, vol. 47, no. 1, pp. 123–132, 1999. [Online]. Available: <https://doi.org/10.1109/78.738245>
- [28] T. M. Cover and J. A. Thomas, *Elements of Information Theory*, 2nd ed. Wiley, 2006.
- [29] H. H. Pennes, “Analysis of tissue and arterial blood temperatures in the resting human forearm,” *J. Appl. Physiol.*, vol. 1, no. 2, pp. 93–122, 1948. [Online]. Available: <https://doi.org/10.1152/jappl.1948.1.2.93>

- [30] J. S. Camilleri, L. Farrugia, S. Curto, D. B. Rodrigues, L. Farina, G. C. Dingli, J. Bonello, I. Farhat, and C. V. Sammut, “Review of thermal and physiological properties of human breast tissue,” *Sensors*, vol. 22, no. 10, p. 3894, 2022. [Online]. Available: <https://doi.org/10.3390/s22103894>
- [31] R. E. Rosensweig, “Heating magnetic fluid with alternating magnetic field,” *J. Magn. Magn. Mater.*, vol. 252, pp. 370–374, 2002, proceedings of the 9th International Conference on Magnetic Fluids. [Online]. Available: [https://doi.org/10.1016/S0304-8853\(02\)00706-0](https://doi.org/10.1016/S0304-8853(02)00706-0)
- [32] L. Néel, “Influence of thermal fluctuations on the magnetization of very fine ferromagnetic grains,” *C. R. Hebd. Seances Acad. Sci.*, vol. 228, no. 8, pp. 664–666, 1949.
- [33] W. F. B. Jr., “Thermal fluctuations of a single-domain particle,” *Physical Review*, vol. 130, no. 5, pp. 1677–1686, June 1963. [Online]. Available: <https://doi.org/10.1103/PhysRev.130.1677>
- [34] G. Singh, N. Kumar, and P. K. Avti, “Computational evaluation of effectiveness for intratumoral injection strategies in magnetic nanoparticle assisted thermotherapy,” *Int. J. Heat Mass Transf.*, vol. 148, p. 119129, 2020. [Online]. Available: <https://doi.org/10.1016/j.ijheatmasstransfer.2019.119129>
- [35] B. Kos, P. Voigt, D. Miklavcic, and M. Moche, “Careful treatment planning enables safe ablation of liver tumors adjacent to major blood vessels by percutaneous irreversible electroporation (ire),” *Radiology and Oncology*, vol. 49, no. 3, pp. 234–241, August 21 2015. [Online]. Available: <https://doi.org/10.1515/raon-2015-0031>
- [36] N. Mahesh, N. Singh, and P. Talukdar, “A mathematical model of intratumoral infusion, particle distribution and heat transfer in cancer tumors: In-silico investigation of magnetic nanoparticle hyperthermia,” *Int. J. Therm. Sci.*, vol. 183, p. 107887, 2023. [Online]. Available: <https://doi.org/10.1016/j.ijthermalsci.2022.107887>
- [37] Y. Tang, T. Jin, R. C. C. Flesch, Y. Gao, and M. He, “Effect of nanofluid distribution on therapeutic effect considering transient bio-tissue temperature during magnetic hyperthermia,” *J. Magn. Magn. Mater.*, vol. 517, p. 167391, 2021. [Online]. Available: <https://doi.org/10.1016/j.jmmm.2020.167391>
- [38] N. Mahesh, N. Singh, and P. Talukdar, “Investigation of a breast cancer magnetic hyperthermia through mathematical modeling of intratumoral nanoparticle distribution and temperature elevations,” *Therm. Sci. Eng. Prog.*, vol. 40, p. 101756, 2023. [Online]. Available: <https://doi.org/10.1016/j.tsep.2023.101756>
- [39] X. Li, B. M. Dawant, E. B. Welch, A. B. Chakravarthy, L. Xu, I. Mayer, M. Kelley, I. Meszoely, J. Means-Powell, J. C. Gore, and T. E. Yankeelov, “Validation of an algorithm for the nonrigid registration of longitudinal breast mr images using realistic phantoms,” *Medical Physics*, vol. 37, no. 6Part1, pp. 2541–2552, 2010. [Online]. Available: <https://doi.org/10.1118/1.3414035>
- [40] S. Martinez and F. Bullo, “Optimal sensor placement and motion coordination for target tracking,” *Automatica*, vol. 42, pp. 661–668, 2006. [Online]. Available: <https://doi.org/10.1016/j.automatica.2005.12.018>

- [41] J. L. Williams, J. W. Fisher, and A. S. Willsky, “Approximate dynamic programming for communication-constrained sensor network management,” *IEEE Trans. Signal Process.*, vol. 55, no. 8, pp. 4300–4311, 2007. [Online]. Available: <https://doi.org/10.1109/TSP.2007.896099>
- [42] R. Madankan, P. Singla, and T. Singh, “Parameter estimation of atmospheric release incidents using maximal information collection,” in *Dynamic Data-Driven Environmental Systems Science*, S. Ravela and A. Sandu, Eds. Cham: Springer International Publishing, 2015, pp. 310–321. [Online]. Available: https://doi.org/10.1007/978-3-319-25138-7_28
- [43] C. P. Robert and G. Casella, *Monte Carlo Statistical Methods*. Springer, 1999.
- [44] H. Niederreiter, *Random Number Generation and Quasi-Monte Carlo Methods*. Society for Industrial and Applied Mathematics, 1992.
- [45] I. H. Sloan and S. Joe, *Lattice Methods for Multiple Integration*. Clarendon Press, 1994.
- [46] P. van Dooren and L. de Ridder, “An adaptive algorithm for numerical integration over an n-dimensional cube,” *J. Comput. Appl. Math.*, vol. 2, no. 3, pp. 207–217, 1976. [Online]. Available: [https://doi.org/10.1016/0771-050X\(76\)90005-X](https://doi.org/10.1016/0771-050X(76)90005-X)
- [47] A. R. Barron, “Approximation and estimation bounds for artificial neural networks,” *Mach. Learn.*, vol. 14, no. 1, pp. 115–133, 1994. [Online]. Available: <https://doi.org/10.1007/BF00993164>
- [48] D. R. Cavagnaro, J. I. Myung, M. A. Pitt, and J. V. Kujala, “Adaptive design optimization: A mutual information-based approach to model discrimination in cognitive science,” *Neural Comput.*, vol. 22, no. 4, pp. 887–905, 2010. [Online]. Available: <https://doi.org/10.1162/neco.2009.02-09-959>
- [49] P. K. Jha, C. Walker, D. Mitchell, J. T. Oden, D. Schellingerhout, J. A. Bankson, and D. T. Fuentes, “Mutual-information based optimal experimental design for hyperpolarized ^{13}C -pyruvate mri,” *Sci. Rep.*, vol. 13, no. 1, p. 18047, 2023. [Online]. Available: <https://doi.org/10.1038/s41598-023-44958-y>
- [50] L. Paninski, “Estimation of entropy and mutual information,” *Neural Computation*, vol. 15, no. 6, pp. 1191–1253, 2003. [Online]. Available: <https://doi.org/10.1162/089976603321780272>
- [51] H. Carlton and R. Ivkov, “A new method to measure magnetic nanoparticle heating efficiency in non-adiabatic systems using transient pulse analysis,” *J. Appl. Phys.*, vol. 133, no. 4, p. 044302, 2023. [Online]. Available: <https://doi.org/10.1063/5.0131058>
- [52] R. Madankan, W. Stefan, S. J. Fahrenholtz, C. J. MacLellan, J. D. Hazle, R. J. Stafford, J. S. Weinberg, G. Rao, and D. Fuentes, “Accelerated magnetic resonance thermometry in the presence of uncertainties,” *Phys. Med. Biol.*, vol. 62, no. 1, p. 214, 2016. [Online]. Available: <https://doi.org/10.1088/1361-6560/62/1/214>
- [53] D. P. Mitchell, K.-P. Hwang, J. A. Bankson, R. J. Stafford, S. Banerjee, N. Takei, and D. Fuentes, “An information theory model for optimizing quantitative magnetic resonance imaging acquisitions,” *Phys. Med. Biol.*, vol. 65, no. 22, p. 225008, 2020. [Online]. Available: <https://doi.org/10.1088/1361-6560/abb9f6>

- [54] A. Kumar, A. Attaluri, R. Mallipudi, C. Cornejo, D. Bordelon, M. Armour, K. Morua, T. L. DeWeese, and R. Ivkov, "Method to reduce non-specific tissue heating of small animals in solenoid coils," *Int. J. Hyperthermia*, vol. 29, no. 2, pp. 106–120, 2013. [Online]. Available: <https://doi.org/10.3109/02656736.2013.764023>
- [55] A. Attaluri, S. K. Kandala, H. Zhou, M. Wabler, T. L. DeWeese, and R. Ivkov, "Magnetic nanoparticle hyperthermia for treating locally advanced unresectable and borderline resectable pancreatic cancers: the role of tumor size and eddy-current heating," *Int. J. Hyperthermia*, vol. 37, no. 3, pp. 108–119, 2020. [Online]. Available: <https://doi.org/10.1080/02656736.2020.1798514>